

RECOMBINATION RATE COEFFICIENT MEASUREMENTS
IN THE HELIUM AFTERGLOW

APPROVED:

L. J. Bonnell Jr.
Major Professor

Carl B. Collins Jr.
Research Professor

W. D. Deering
Minor Professor

L. J. Bonnell Jr.
Director of the Department of Physics

Robert B. Toulouse
Dean of the Graduate School

RECOMBINATION RATE COEFFICIENT MEASUREMENTS
IN THE HELIUM AFTERGLOW

THESIS

Presented to the Graduate Council of the
North Texas State University in Partial
Fulfillment of the Requirements

For the Degree of

MASTER OF ARTS

By

William E. Wells, Jr., B. A.

Denton, Texas

August, 1969

PREFACE

This thesis describes a method of determining the recombination rate coefficient experimentally, which does not depend on a specific model of the recombination process. With this method established, results are presented for the recombination rate coefficient measurements at 44.6 Torr. It is anticipated that as a result of this method, the recombination rate coefficient can be determined at various pressures and electron densities, and the effects of the various constituent processes of recombination and reionization on the recombination rate coefficient studied. Of particular interest will be the determination of the effect of neutrally assisted recombination at high pressures. Although this has been theoretically predicted, it is yet to be experimentally observed.

The author would like to acknowledge the guidance, advice and many helpful discussions generously given to the author by his research professor, Dr. C. B. Collins, of the Southwest Center for Advanced Studies. The Southwest Center for Advanced Studies has provided the author with all necessary equipment and a conducive atmosphere for research, for which the author is grateful.

Finally, the author wishes to express his gratitude

to the National Science Foundation and the National Aeronautics and Space Administration for their financial support.

TABLE OF CONTENTS

	Page
PREFACE	i
LIST OF TABLES.iv
LIST OF ILLUSTRATIONS	v
Chapter	
I. INTRODUCTION	1
II. THE HELIUM AFTERGLOW.	4
III. RECENT MEASUREMENTS OF THE RECOMBINATION RATE COEFFICIENT IN HIGH PRESSURE HELIUM13
IV. A NEARLY MODEL-INDEPENDENT MEASUREMENT OF THE RECOMBINATION RATE COEFFICIENT16
V. APPARATUS AND TECHNIQUES19
VI. EXPERIMENTAL RESULTS.34
VII. CONCLUSIONS.48
REFERENCES50
APPENDIX A52

LIST OF TABLES

Table	Page
I. Gas Impurities in the 44.6 Torr Helium Afterglow Cell.	20

LIST OF ILLUSTRATIONS

Figure	Page
1. An Energy Level Diagram of Atomic Helium, Illustrating the Electron Energy Levels.	10
2. A Drawing of the Quartz Afterglow Used in the Recombination Rate Coefficient Measurement.	22
3. A Representational Diagram of the Gas Handling System.	24
4. A Block Diagram of the Photon Counting and Data Acquisition System.	27
5. A Block Diagram of the 36GHz Microwave Interferometer and Data Acquisition System.	32
6. A Graph of Photon Emission Rates.	36
7. Total Photon Emission Rate Measured as a Function Time.	38
8. A Graph of the Product Concentrations $[\text{He}^+][e]$ in Units of cm^{-6} Measured as a Function of Time in msec.	41
9. A Graph of the Recombination Rate Coefficient, α , in Units of $\text{cm}^3\text{sec}^{-1}$, Plotted as a Function of Time in msec.	43
10. A Graph of Electron Density in Units of cm^{-3} Versus Time in msec.	45

Figure	Page
11. A Graph of the Recombination Rate Coefficient Measured as a Function of Electron Density, at a Neutral Gas Pressure of 44.6 Torr.47
12. Diagram of Calibration Setup Used to Determine Absolute Intensity.	54

CHAPTER I

INTRODUCTION

The study of ion-electron recombination was first begun by Thomson and Rutherford in the late nineteenth century. From that time to the present, it has been an area of fundamental study in atomic physics.

Only recently has an understanding of the basic constituent processes involved in this phenomena been developed and models constructed to represent the recombination. However, because of the difficulties involved in making independent measurements of all of the parameters of the total recombination process, most of the measurements involve use of the models dictated by the processes. Naturally, the accuracy of such measurements is limited by the accuracy of the models used.

This paper describes a technique for a nearly model-independent measurement of the rate coefficient for recombination, and provides an unbiased representation of the recombination.

Helium provides a natural medium for the study of the recombination of ions and electrons. Its structure, surpassed in simplicity only by hydrogen, presents a simple spectrum for analysis. Unlike hydrogen, helium's lowest

energy state is that of an atom, rather than a molecule, and it does not react to form stable molecules. For these reasons, it was chosen as the demonstration medium for the technique described in this paper.

Being the inverse of ionization, ion-electron recombination is an exothermic reaction and can be best observed in an energetically isolated system. For this reason, the afterglow period of a plasma discharge is the optimum time to observe the ion-electron recombination. In this period there are no external energy sources which result in ionization. Any ionization which does occur during this period must be from internal sources and be a part of the recombination process.

A brief description of the recombination processes in the helium afterglow, along with the definitions of the pertinent parameters of the afterglow, can be found in Chapter II. Recent measurements of the recombination rate coefficient of helium are cited and reviewed in Chapter III. In Chapter IV, the concept of this experiment is described, and the assumptions to be used in interpreting it are justified. The experimental techniques and apparatus utilized during the course of this experiment are described in Chapter V.

To test the merit of this method of measurement, the recombination rate coefficient as a function of electron density was determined for a pressure of 44.6 Torr. The

result of this measurement is found in Chapter VI. Conclusions regarding the use of this new measurement technique, and its relevance in determining the importance of one type of recombination, those which are neutrally stabilized, are discussed in Chapter VII. Calibration techniques utilized to determine absolute intensities of the individual spectroscopic observations are discussed in Appendix A.

CHAPTER II

THE HELIUM AFTERGLOW

A plasma may be created by imposition of an electric field on a region containing neutral atoms and/or molecules, thereby ionizing a significant fraction of them. Although helium is normally monatomic, after an electric field is discharged through the gas and ionization has occurred, helium molecular ions, as well as helium atomic ions, are formed. The molecular ions are formed by the three-body reaction, where X is the third body,



which is very probable during the afterglow, especially at high neutral particle densities. Here, for the purpose of discussion, an arbitrary differentiation between high- and low-density plasmas will be made at a pressure of 3 Torr.

Both types of ions are subject to recombination, and after recombination, can relax to metastable states. The metastable states, in the case of the atomic ion, have very low probabilities of radiative transitions to the ground state; and in the case of the molecular ion, a bound lower state does not exist. Both atomic and molecular metastables must depend primarily on collisions which absorb enough energy to place them in the atomic ground state or

excite them to a state which has an open radiative channel to the ground state. At high pressures, significant concentrations of metastables are formed and collisions of the metastables with themselves, and other constituents of the plasma, become very probable. These collisions not only provide a means of relaxing the metastables to the atomic ground state, but can have the opposite effect. If energetic enough, the collisions can cause reionization. Thus, during the afterglow, a source of reionization can be created as a byproduct of recombination.

Unless a plasma is completely uniform, so that no density gradient exists, the ions and electrons diffuse from the regions of high density to a lower density region. Because of the electric forces which exist between the charges, they do not diffuse at their individual rates. Schottky¹ has shown the electrons and ions to diffuse at the same rate, even though they have different mobilities, K , and diffusion coefficients, D . He found the diffusion of both could be described by a common diffusion coefficient,

$$D_a = (D^+K^- + D^-K^+) / (K^+ + K^-), \quad (2)$$

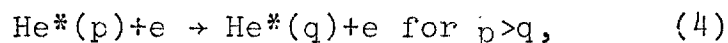
where the + and - superscripts refer to the positive and negative ions, respectively.

The process of recombination starts as the first ions are formed and continues throughout the maturity of the afterglow. Generally it can be subdivided into two groups, those which are electron stabilized and those which are

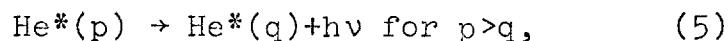
neutrally stabilized. Bates, Kingston, and McWhirter², and Hinnov and Hirschberg³ have developed the collisional radiative theory based on the model described by



The atom is subsequently relaxed by the process,

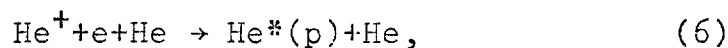


which dominates for high principal quantum numbers, p and q , and by

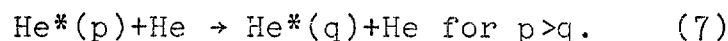


which dominates for low quantum numbers. In the above processes, the asterisk denotes an excited state. Process (5) describes the case where the energy of the relaxation of the atom is given off in the form of a photon of energy equal to $h\nu$. Here h is Plank's constant and ν is the frequency of radiation.

Bates and Khare⁴ have also considered the model of recombination,



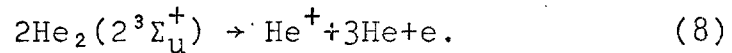
which has in addition to the processes of relaxation (5) and (6), also the process,



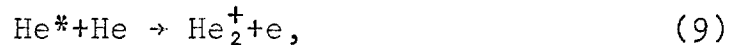
Collins⁵ has theoretically treated processes (3) and (6), and has shown the dominance of process (6) at high neutral densities and low electron densities. An experimental verification of this dependence has not yet been observed.

Molecular helium is believed to recombine⁶ in a fashion similar to the collisional radiative atomic recombination model.

The importance of sources of ionization in the afterglow has only recently been experimentally observed^{7, 8}. Collins and Hurt^{7, 8} have extended the observation period of an afterglow from a few hundred μsec to 50 msec. The data resulting from this extended observation period indicated an important late time source of ionization. This source was shown to be compatible with the reaction,



In addition to this reionization source, two other proposed sources are the Hornbeck-Molnar process⁹,



and the process of electron attachment¹⁰,



Electron attachment in helium is very improbable, due to the inert character of the atom, and can be ignored, but the other two processes can form significant sources of ionization and affect the net recombination.

The conversion of He^+ to He_2^+ , and the return, indirectly, of the He_2^+ to He^+ , complicates the recombination and leads to three coupled differential equations, which describe the recombination. When the effect of diffusion, as described by the ambipolar diffusion coefficient and the Laplacian of the density, is also taken into account,

these equations are

$$d[\text{He}^+]/dt = D_{1a} \nabla^2 [\text{He}^+] - \alpha_1 [\text{He}^+] [e] - \beta [\text{He}^+], \quad (11)$$

$$d[\text{He}_2^+]/dt = D_{2a} \nabla^2 [\text{He}_2^+] - \alpha_2 [\text{He}_2^+] [e] + \beta [\text{He}^+], \quad (12)$$

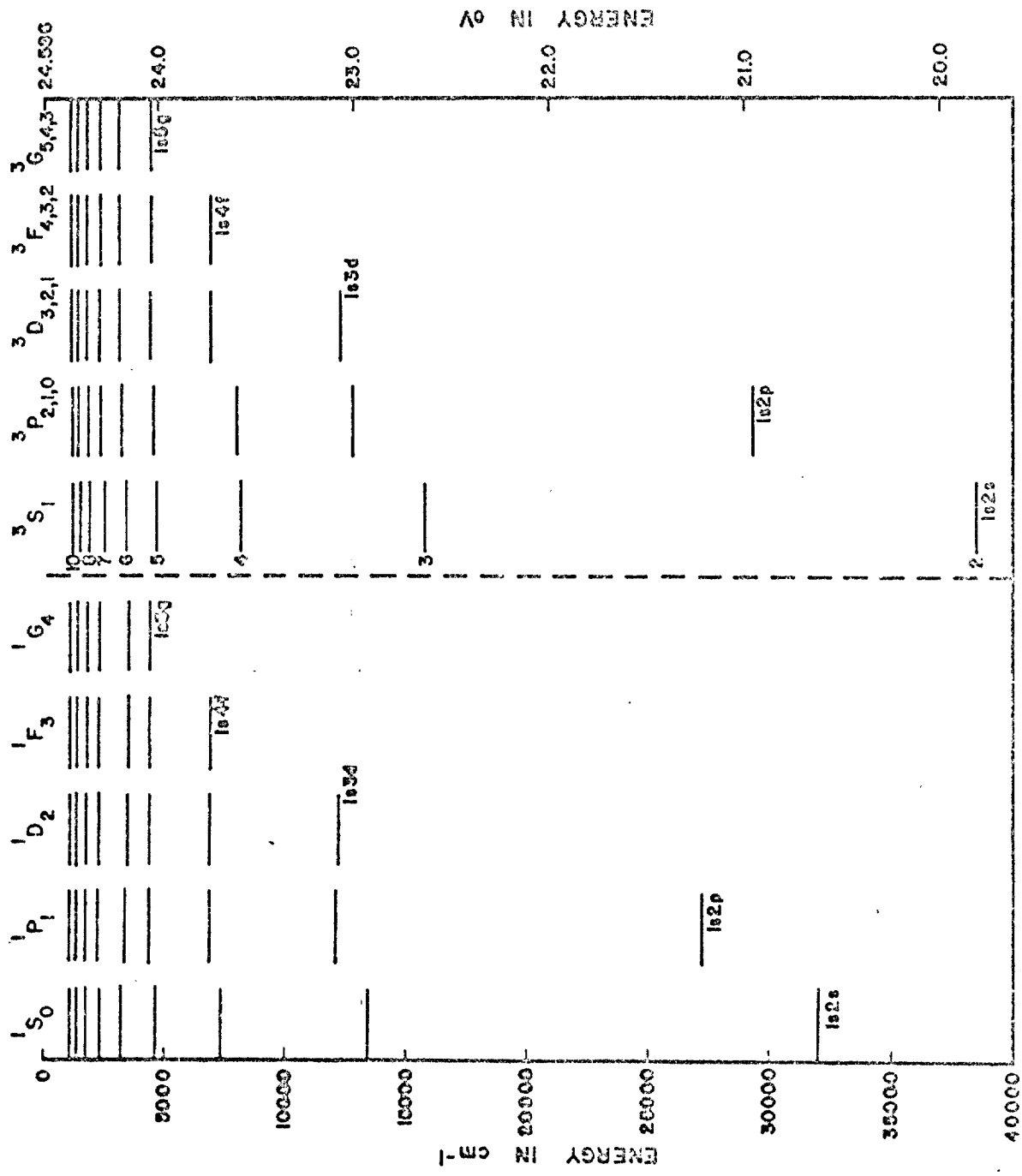
$$d[e]/dt = [(D_{1a} [\text{He}^+] + D_{2a} [\text{He}_2^+]) / ([\text{He}^+] + [\text{He}_2^+])] \nabla^2 [e] - \alpha_1 [\text{He}^+] [e] - \alpha_2 [\text{He}_2^+] [e], \quad (13)$$

where the recombination rate coefficient is represented by α . The probability of converting He^+ to He_2^+ is represented by β , and the brackets indicate ion densities. The subscripts 1 and 2 refer to He and He_2 , respectively.

Equations (11), (12), and (13) account for the gain and loss of ions due to diffusion, recombination and atomic to molecular ion conversion. But these do not contain the internal sources of ionization. Any of the processes, such as (8) and (9), which lead to reionization will add gain and loss terms to the appropriate equations.

The quantum nature of the atom only allows specific energy levels to exist within the atom, as depicted in Figure 1. Each energy level is labeled by its electron configuration in spectroscopic notation.

As an excited atom is relaxed to the ground state, it may undergo several transitions to intermediate states before finally making the transition to the ground state. Because of the selection rules, there are only six series of transitions to the $n = 2$ level. The $n = 2$ level is important, because at this level reionization is extremely improbable, and the electron can be considered to be stably



bound. These series of transitions are

$$n^1P \rightarrow 2^1S,$$

$$n^1S \rightarrow 2^1P,$$

$$n^1D \rightarrow 2^1P,$$

$$n^3S \rightarrow 2^3P,$$

$$n^3P \rightarrow 2^3S,$$

and
$$n^3D \rightarrow 2^3P. \quad (14)$$

For each state, n , of excitation of the atom, a probability of reionization, P_n , can be assigned, which will increase with n because of the lower amount of energy required to achieve ionization. The probability of recombination to quantum level n , R_n , is also an increasing function of n . The number of recombinations into state n is

$$I_+ = R_n[\text{He}^+], \quad (15)$$

and the number of reionizations out of state n is

$$I_- = P_n[\text{He}(n)]. \quad (16)$$

There is a state n , where

$$I_+ \sim I_-, \quad (17)$$

indicating an equilibrium between the free electrons and the state n . All states where q is larger than n will also be in equilibrium. This occurs because $[\text{He}(q)]$ will increase or decrease until the equilibrium exists.

Saha¹¹ derived a thermodynamic equilibrium relationship based on Boltzmann's¹¹ work which relates the population of an excited state to that of the continuum, and is

important in recombination because it shows the relationship of excited state populations to the ion and electron populations. In the case of atomic helium, the Saha equation is

$$[\text{He}^+][e] = [\text{He}(n)](g^+ g_e / g_n)(2mKT/h^2)\exp(-U_n/KT) \quad (18)$$

where g^+ , g_e and g_n are the statistical weights of the ion, electron, and excited neutral atom, respectively. The mass of the electron is represented by m and Boltzmann's constant by K . T represents the temperature. The ionization energy of the state n is U_n .

CHAPTER III

RECENT MEASUREMENTS OF THE RECOMBINATION RATE COEFFICIENT IN HIGH-PRESSURE HELIUM

Most of the measurements of the recombination rate coefficient have been made at low pressures, as defined in the previous chapter, and agree quite well with the collisional radiative recombination theory^{2, 3}. However, two recent measurements which extend into the high-pressure region, where neutrally assisted recombination could occur, are the experiments of Born^{1,2}, and Deloche, Gonfalone, and Cheret^{1,3}.

Born^{1,2} made his measurements from 0.25 Torr to 20 Torr, with a notable gap between 2.7 Torr and 12.5 Torr. Although he does not explain in his paper how his recombination rates were determined, from the data displayed and his justifications for the rates, the following appears to have been the method of determination. At low pressures, the $[\text{He}^+]$, helium atomic ion concentration, dominates over the $[\text{He}_2^+]$, helium molecular ion concentration. At high pressures, the $[\text{He}_2^+]$ dominates over the $[\text{He}^+]$. By invoking charge neutrality,

$$[e] = [\text{He}^+] + [\text{He}_2^+], \quad (19)$$

the extremes of low and high pressure can be approximated

by

$$[e] \sim [\text{He}^+] \text{ for } p < 3 \text{ Torr,} \quad (20)$$

and

$$[e] \sim [\text{He}_2^+] \text{ for } p > 12 \text{ Torr.} \quad (21)$$

With these assumptions, the coupled equations, (11) and (12), can be considered to be independent, and can be written as

$$d[\text{N}^+]/dt = D_a \nabla^2 [\text{N}^+] - \alpha [\text{N}^+] [e], \quad (22)$$

where N represents the majority ion in the afterglow. From equations (20) and (21), equation (22) can be rewritten as

$$d[e]/dt = D_a \nabla^2 [\text{N}^+] - \alpha [\text{N}^+] [e]. \quad (23)$$

Born presents data in his paper¹² for the intensity of a state in Saha equilibrium and the electron density. The product concentration, $[\text{N}^+][e]$, can be determined from the Saha equation when the population of a state in Saha equilibrium is known. The diffusion term was apparently determined theoretically. With these values known, the value of the recombination rate coefficient can be determined.

Born chose 9^3D state to be in equilibrium with the free electrons. However, Collins and Hurt¹⁴, and subsequently Born and Buser¹⁵, have shown this value to be far too low. From the data presented by both Collins and Hurt, and Born and Buser, principal quantum numbers of 15 or greater should have been chosen. This erroneous choice of the Saha level makes the validity of the measurement questionable, even granting the highly restrictive model used.

Deloche, Gonfalone and Cheret¹³ assumed the model depicted by equations (11), (12) and (13). This represents a significant improvement in the model over the simplest choice of models made by Born.

In order to account for the electronically (9) and neutrally (12) stabilized recombinations, they introduce

$$\alpha = \alpha_0 + k[e], \quad (24)$$

where α_0 represents the recombinations from process (12) and $k[e]$ the recombinations from process (9).

Equations (11), (12), (13), and (24), used in conjunction with the measured loss of electrons, were solved by a process of curve fitting to give the rate coefficients of equation (24).

However, this measurement is also dependent on a model applied to the afterglow, and, of course, can only be as accurate as the model. Sources of reionization, such as (6) and (8), have not been considered in the model. Because of the importance of these mechanisms in the recombination, reservations about the values obtained in this experiment must be maintained until all mechanisms of recombination and ionization are evaluated, or a model-independent measurement of the recombination rate coefficient validates the model used.

CHAPTER IV

A NEARLY MODEL-INDEPENDENT MEASUREMENT OF THE RECOMBINATION RATE COEFFICIENT

In the collisional radiative recombination theory, described in Chapter II, many recombinations occur into the high quantum levels, but only those which are stabilized by relaxation to low quantum levels contribute to the net recombination. The measurement technique, described in this chapter, monitors such radiative relaxations to the $n = 2$ principal quantum level.

Radiative transitions to the ground state were not measured, because this radiation is imprisoned in the plasma and only a small amount escapes. A photon released by a relaxation to the ground state is exactly the amount of energy required to raise a ground state neutral to the energy state previously occupied by the relaxed atom. Since the cell contains primarily neutral atoms in the ground state, there is a high probability of reabsorption of the photon. The newly excited atom has a probability of decaying to the ground state by another path. The probability of escape depends on the neutral density and the geometry of the cell. Holstein¹⁶ has developed a procedure for calculating this probability of escape. Based on this

method, Frost and Phelps¹⁷ calculated the transition probability for the $n^1P \rightarrow l^1S$ transitions as modified by the escape probability for a cylinder 3.0 mm in diameter and a pressure of 1 Torr. This value was $.527 \times 10^6 \text{ sec}^{-1}$.

In the case of this experiment, the cell diameter is 10.2 cm in diameter and has a pressure of 44.6 Torr. Both of these larger parameters would present large reductions in the escape probability for the ground state transitions in the experiment described herein. However, using the above as a limit, less than 0.003% of the transitions to the ground state take place by direct radiative transitions and escape the cell.

As shown in reaction (4), nonradiative transitions to the $n = 2$ level are possible. But, as suggested in Chapter I, these nonradiative transitions are improbable at low principal quantum numbers. During the collision which liberates the excess energy from the excited atom without radiation, the colliding electron increases its kinetic energy. This type collision is called a superelastic collision. The rate coefficient calculated¹⁸ for the electron-collision superelastic de-excitation rate, reaction (4), for the $n = 3$ to $n = 2$ levels of helium, is $6 \times 10^{-9} \text{ cm}^3 \text{ sec}^{-1}$. At maximum electron densities, characteristic of the early afterglow as described in Chapter V, the nonradiative rate of relaxations is limited to

$5 \times 10^3 \text{sec}^{-1}$. The radiative rate for the same transition quoted by Niles¹⁹ is $13 \times 10^6 \text{sec}^{-1}$. Since the most probable nonradiative transition to the $n = 2$ level is from the $n = 3$ level, the ratio of these two rates can be considered as an upper limit for all transitions. Computing in this manner, only .05% of the relaxations to the ground state could proceed by the nonradiative superelastic de-excitation process.

Since the preponderance of transitions to the $n = 2$ level can therefore be assumed radiative, the monitoring of the radiation from the afterglow gives an accurate indication of the recombination events per unit time, R . The recombination events per unit time, R , is related to $d[\text{He}^+]/dt$ of equation (3) by

$$R = d[\text{He}^+]/dt - D_a \nabla^2 [\text{He}^+] + \beta [\text{He}^+], \quad (25)$$

because R is an indication of the recombination to the atomic state and does not include loss due to diffusion or conversion to the molecular ion. A simplified expression,

$$R = -\alpha [\text{He}^+][e], \quad (26)$$

results when substituting equation (11) into equation (26).

The Saha equation relates the product density with the free electrons. When this value is obtained, the recombination rate coefficient, α , is easily determined by

$$\alpha = -R/[\text{He}^+][e]. \quad (27)$$

CHAPTER V

APPARATUS AND TECHNIQUES

A cylindrical quartz cell 17.5 cm in length, depicted in Figure 2, was used to contain the afterglow. Tantalum electrodes were used to provide repetitive power pulses to gas to create the initial discharge.

Special low-neon content (0.2 ppm) helium was admitted to the gas handling system. Cataphoretic pumping²⁰ was used to further purify the gas before introducing it into the cell. Because of the relative high pressure of the gas, temperatures dangerous to the glass tube were developed during the cataphoretic pumping. To eliminate this danger, a glass jacket was constructed around the tube and water was allowed to flow through the jacket, cooling the walls of the tube. With this modification to the standard method of cataphoretic pumping, there was no difficulty in obtaining very pure helium. Table 1 lists the impurities which were found spectroscopically and their intensity level, as compared to the peak intensity of the 4650 Angstrom molecular band of helium. Figure 3 shows a representational diagram of the gas handling system utilized. The final gas pressure in the cell was 44.6 Torr.

TABLE I
 GAS IMPURITIES IN THE 44.6 TORR
 HELIUM AFTERGLOW CELL

Impurity	Observation Wave Length In Angstroms	Ratio* Of Intensity
CO+	4274.3	No Trace
H	4861.3	.02
N ₂ ⁺	4278	No Trace
Ne	5850	.017

* The intensity of the impurity was compared to the peak intensity of the 4650-Angstrom helium molecular band, by forming a ratio. The ratio of the background intensity to the peak intensity of the 4650-Angstrom helium molecular band was .01.

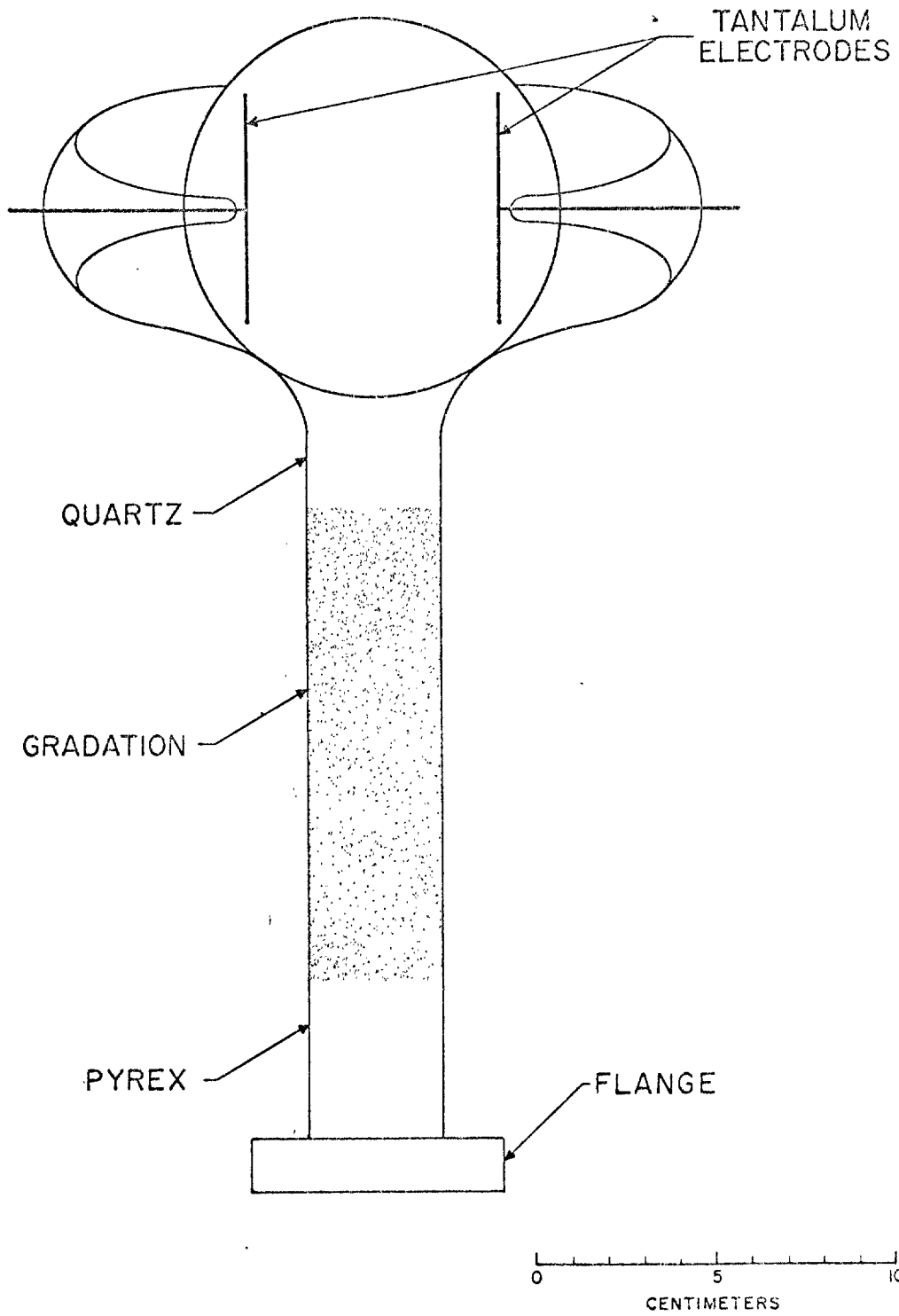
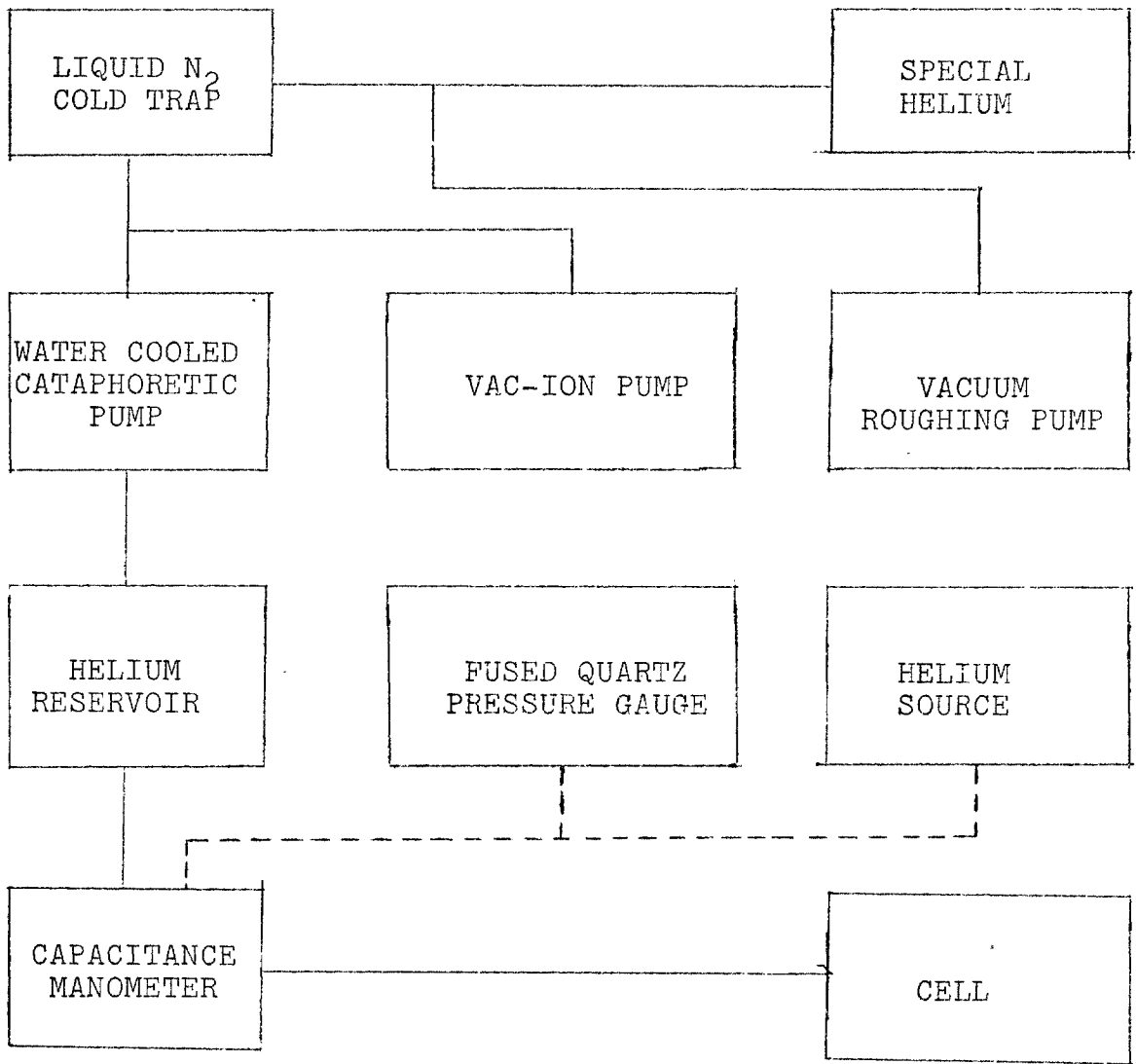


Figure 3

A representational diagram of the gas handling system.



— indicates primary manifold.

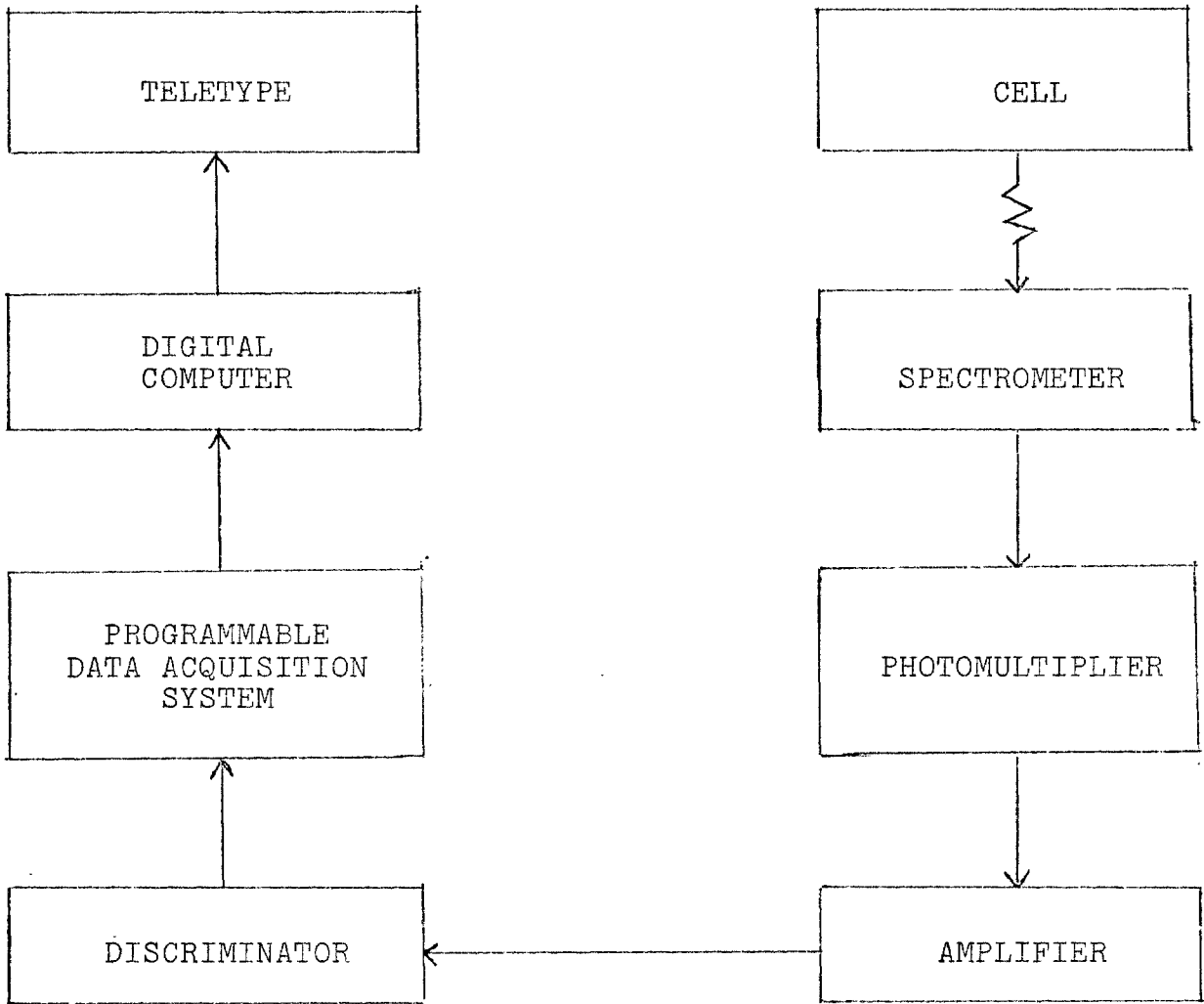
- - - indicates secondary manifold.

A low level pulse generator synchronized to a data acquisition system was used to trigger a high-voltage pulse generator. In standard operation, the cell was pulsed with 5000 volts for 10 μ sec 16 times per second. Several tens of thousands of periods of afterglow were needed to achieve statistically good data.

Figure 4 shows a block diagram of the photon counting and data acquisition system. In the visible region, the spectrometer used was a Czerny-Turner .75-meter tandem spectrometer. In quartz ultraviolet and infrared regions of the spectrum, data was acquired with a .5-meter Ebert spectrometer. An EMI 6256S photomultiplier was utilized to detect the photons passed by the spectrometer. After amplification of the output pulses, they were processed by a discriminator with an adjustable discrimination level, which was optimized for maximum signal detection and dark current rejection. A programmable data acquisition system then accumulated the conditioned pulses, in phase increments of time width determined by the program. The system could accommodate a maximum of 500 frames of data per afterglow cycle. The framing scheme utilized for this experiment was nineteen 10- μ sec frames, followed by ninety-six 25- μ sec frames, and then, one hundred twenty 500- μ sec frames. This scheme, with short frames during the early time periods and long frames during the late time periods, allowed adequate time resolution when the count rates were high, and the

Figure 4

A block diagram of the photon counting and data acquisition system.



slope of the data was also high. Poorer time resolution occurred where time resolution was not as important, but total counts accumulated in a frame were important in order to minimize statistical errors. In the late time regions, the slope is low and slowly changing; therefore time resolution is not as important. Examples of this framing scheme are presented in Chapter VI.

The number of photon counts in each frame was converted to a photon count rate by an on-line digital computer. The last 5 msec of data, corresponding to approximately 60 msec into the afterglow, were averaged together to form a base line reference. The data was then adjusted to this base line. Using standard statistical methods, the number of counts in each frame was used to calculate the standard deviation of the data.

All spectroscopic observations of relaxations from one excited state to another were compared to a known radiation source, supplied by the Bureau of Standards. Utilizing this standard, an allowance for the efficiency of the spectrometer was made to adjust the data to a true photon count rate incident on the spectrometer slits. Then, from the geometry of the optical path, the observed solid angle of radiation was determined. This calibration is discussed further in Appendix A. From this data, the total radiation from the cell could be determined for a particular wave

length, and hence the total rate of relaxation to one state from another state, represented by observed wavelength, was determined.

The digital computer was utilized to add all of the data, for the six series of transitions taken, together, frame by frame. For each series, data was taken on transitions up to the quantum level, where each new addition to the total was two orders of magnitude lower in count rate than the total. This sum then represented the total relaxations to the $n = 2$ states of the helium atom.

Data was also taken on the $15^3P \rightarrow 2^3S$ transition, which was assumed to be in Saha equilibrium with the continuum. Equation (18) was then applied to this data, again on a frame-by-frame basis, to indicate the product concentration of $[\text{He}^+][e]$ as a function of time. Because this radiation was in the quartz ultra-violet region, 2634 Angstroms, and of very low intensity, two runs of data were required, the first, an observation of 2634 Angstroms, and the second, an observation of 2634 Angstroms with a filter to absorb the ultra-violet radiation and transmit the visible and infrared radiation. Subtracting one set of data from the other removed the scattered light resulting from the intense transitions in the visible and infrared regions. A total of 650 000 sweeps of the afterglow was utilized to obtain this data.

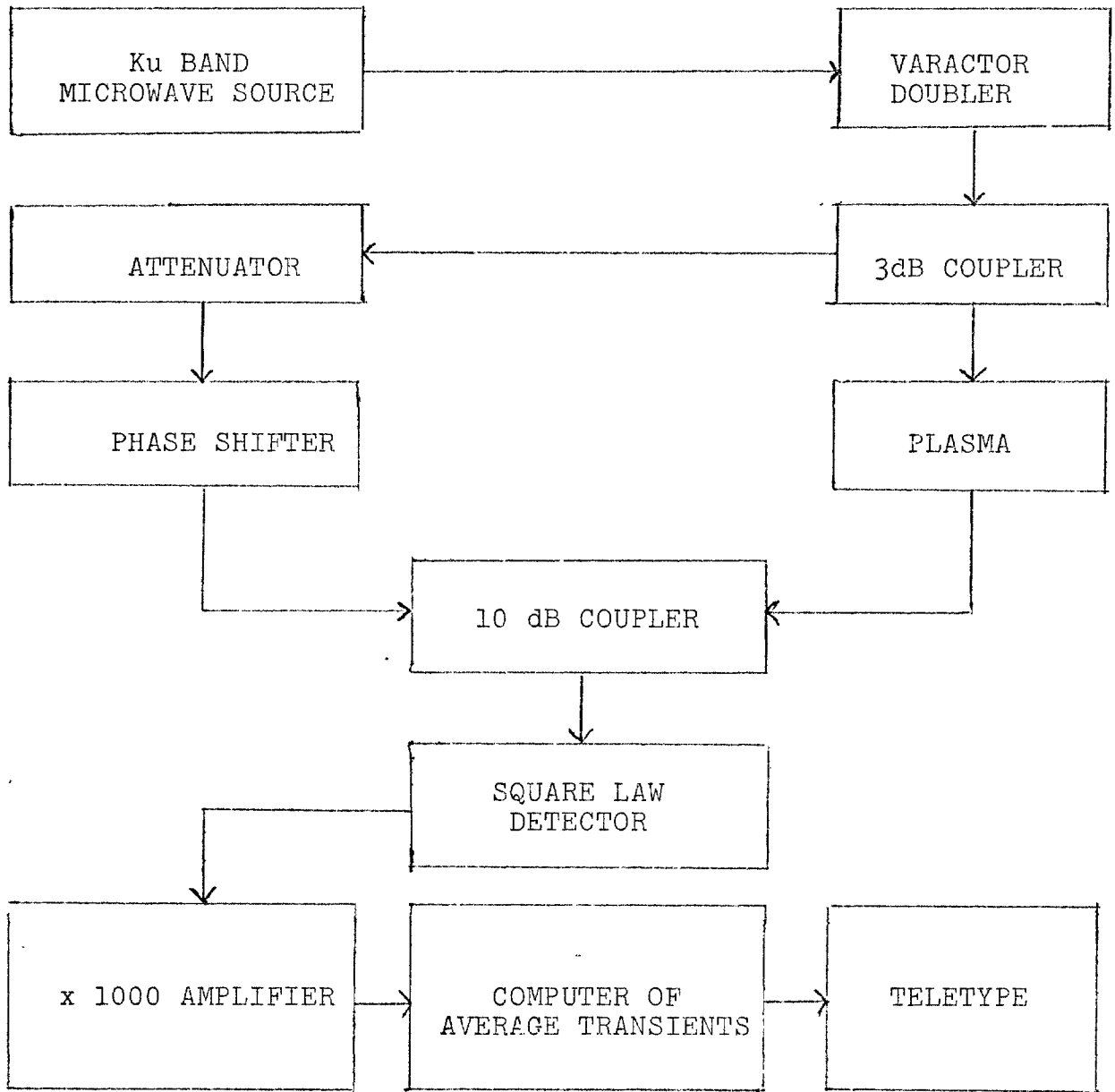
A 35 GHz microwave interferometer was employed to determine the phase shift within the plasma as a function of time. The electron densities were calculated²¹, utilizing the difference in phase shift, $\Delta\phi$, between a microwave path which is constant in phase and one in which the microwave energy propagates through the plasma. The electron density, averaged over the plasma path, is

$$[e] = 2\epsilon_0 mc\omega\Delta\phi/e^2, \quad (28)$$

where ϵ_0 is permittivity of free space and m is the mass of the electron. The angular frequency of the microwave energy is represented by ω and e is the charge of the electron.

Figure 5 is a representational diagram of the interferometer and the data acquisition system. The microwave test signal was developed by a Ku band sweep generator set at 18 GHz. This signal was doubled to 36 GHz by a varactor doubler. Then, the signal was split into two paths which contained two microwave horn antennas which allow propagation of the microwave signal through the cell. The two paths were rejoined in a 10-dB top-wall coupler, and detected by a crystal detector in a waveguide mount. The detected signal was then amplified by a factor of 1000 and accumulated by phase in a computer of average transients.

The same data acquisition system as was used for the spectroscopic data could not be used, because the crystal



detector produces an analog signal, while the photomultiplier produces a digital signal. The framing scheme used for this measurement differed from the spectroscopic framing because of the equipment used to accommodate the analog signal. The minimum frame phase length available was 78 μ sec, and a maximum of only 200 of these could be handled during each afterglow cycle.

Since the frame sizes of the electron density data and the spectroscopic data were different, all of the spectroscopic data was reframed on the digital computer to correspond to the larger frame size of the electron density.

Because the total relaxation rate to the $n = 2$ level represent the total number of recombination events per unit time, this data, along with the $[\text{He}^+][e]$ product density, was introduced into the equation (27), and the recombination rate coefficient determined as a function of time. Having determined both $[e]$ and α as functions of time, they can be related to each other by the elimination of the parameter time.

CHAPTER VI

EXPERIMENTAL RESULTS

In Figure 6, the $n^3P \rightarrow 2^3S$ series data are presented. These data indicate the total photon emission rate per unit volume at the center of the cell, from the excited states marked on each curve to the 2^3S metastable state. Forty msec of usable data were obtained for each of the transitions shown. The boxes represent the error in the measurement. The limits of the boxes, parallel to the ordinate, indicate the error inherent in the determination of the time by the framing scheme discussed in Chapter V. The internal lines, parallel to the abscissa, are the statistically determined data. The limits of the boxes in this direction are the errors indicated by the standard deviation of the data. This data, and the data from the other five series, mentioned in Chapter II, were added together to give the total photon emission rate per unit volume, displayed in Figure 7. As stated in Chapter IV, this represents the total recombination events per unit time, per unit volume.

The data from the $15^3P \rightarrow 2^3S$ was extremely weak, and at early times in the afterglow, peak count rates of only 10^3 counts per sec were observed. Only 2.5 msec of usable

Figure 6

A graph of photon emission rates, in units of $\text{cm}^{-3}\text{sec}^{-1}$, from the $n^3\text{P} \rightarrow 2^3\text{S}$ series versus time in msec. The emission represents transitions from $n^3\text{P} \rightarrow 2^3\text{S}$. Each level $n^3\text{P}$ is labeled on the graph.

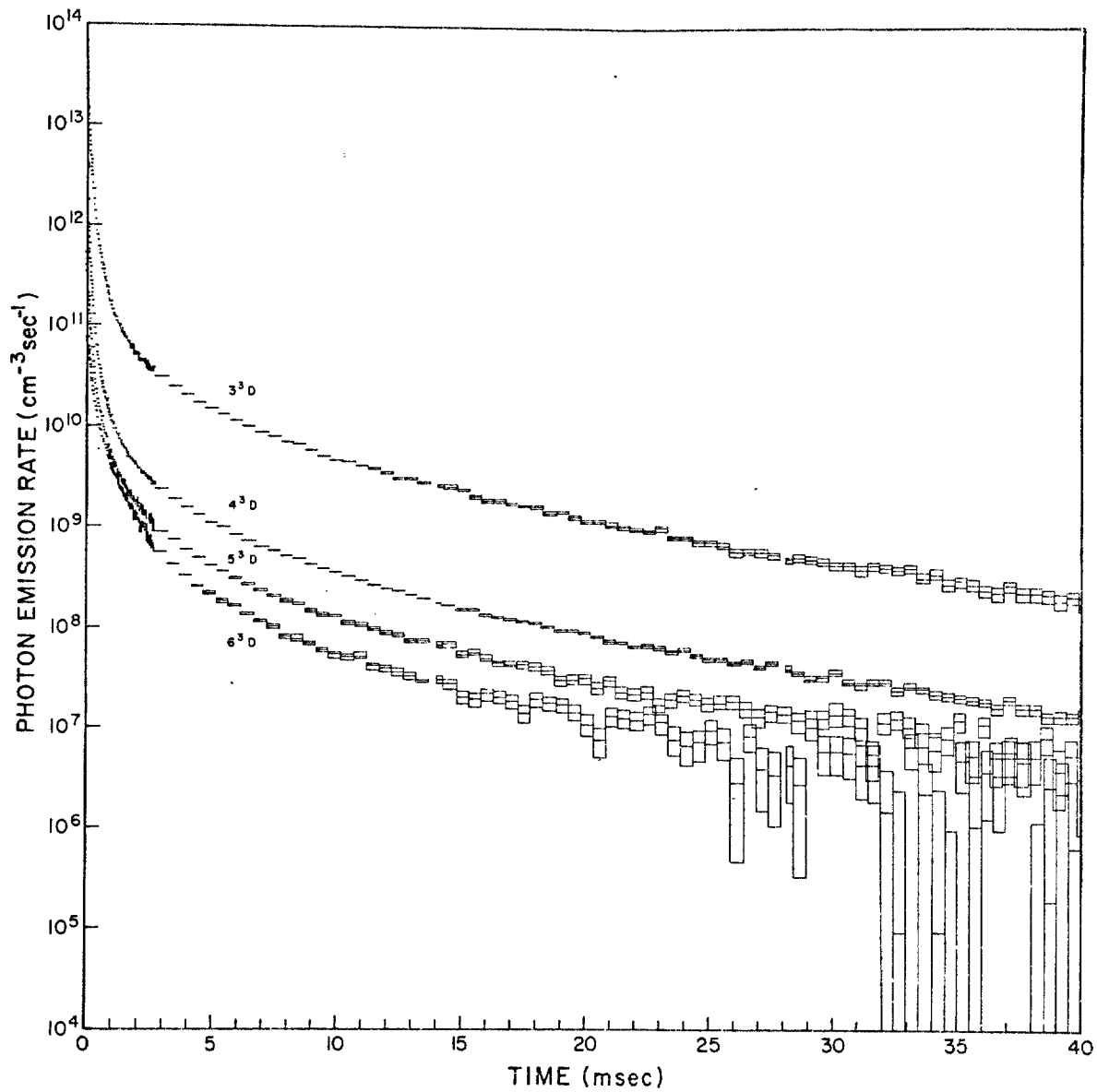
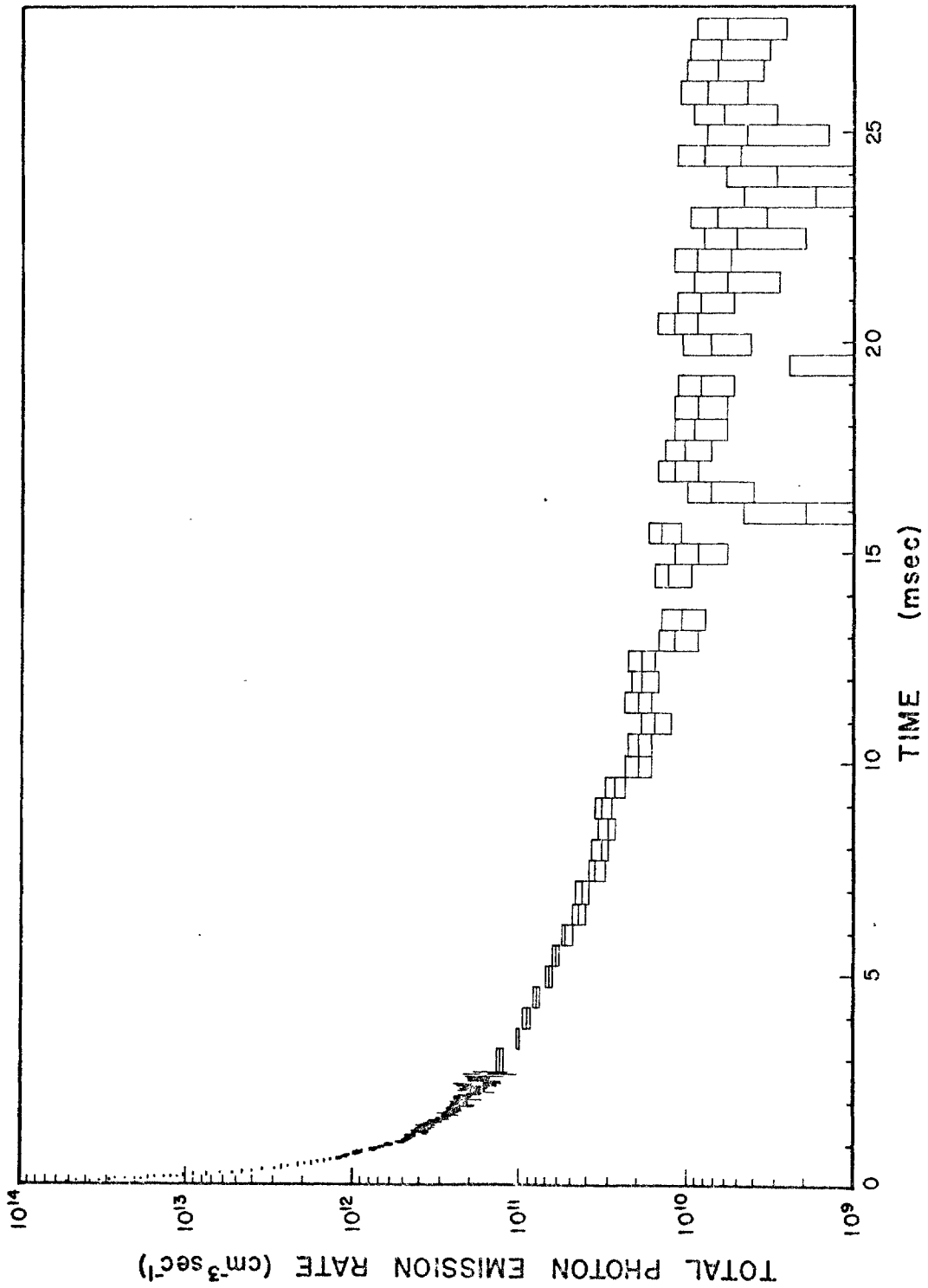


Figure 7

Total photon emission rate ($\text{cm}^{-3}\text{sec}^{-1}$) measured as a function of time (msec).



data were obtainable, for over this interval the count rate dropped to the order of 1 count per sec. With the aid of the Saha equation (18), these data were converted to the $[\text{He}^+][e]$ product density, shown in Figure 8.

Equation (27) was applied, frame by frame, to the data which represent the recombination rate of $[\text{He}^+]$ in Figure 7, and the data of Figure 8, which represent $[\text{He}^+][e]$. The result of this operation is displayed in Figure 9 and represents the recombination rate coefficient versus time. These data are severely limited by the data from the $15^3\text{D} \rightarrow 2^3\text{S}$ transition. As a consequence, the recombination rate coefficient could only be determined to 3.5 msec.

The electron density measurement, as discussed in Chapter V, was made with the 36-GHz microwave interferometer, and this is presented in Figure 10. No method of monitoring the statistical nature of the data was available with existing equipment, so the data are presented without error limits. However, from the smoothness of the data, one can infer a low statistical error.

Figure 11 is a log-log plot of the recombination coefficient versus electron density, where the experimental parameter time, after appropriate reframing of the spectroscopic data, has been eliminated.

Presented also in Figure 11 is a theoretical calculation⁵ of the electron density dependence of the recombination rate coefficient.

Figure 8

A graph of the product concentrations $[\text{He}^+][e]$ in units of cm^{-6} measured as a function of time in msec. This graph was derived from the $15^3\text{D} \rightarrow 2^3\text{P}$ transition and equation (18) in the text.

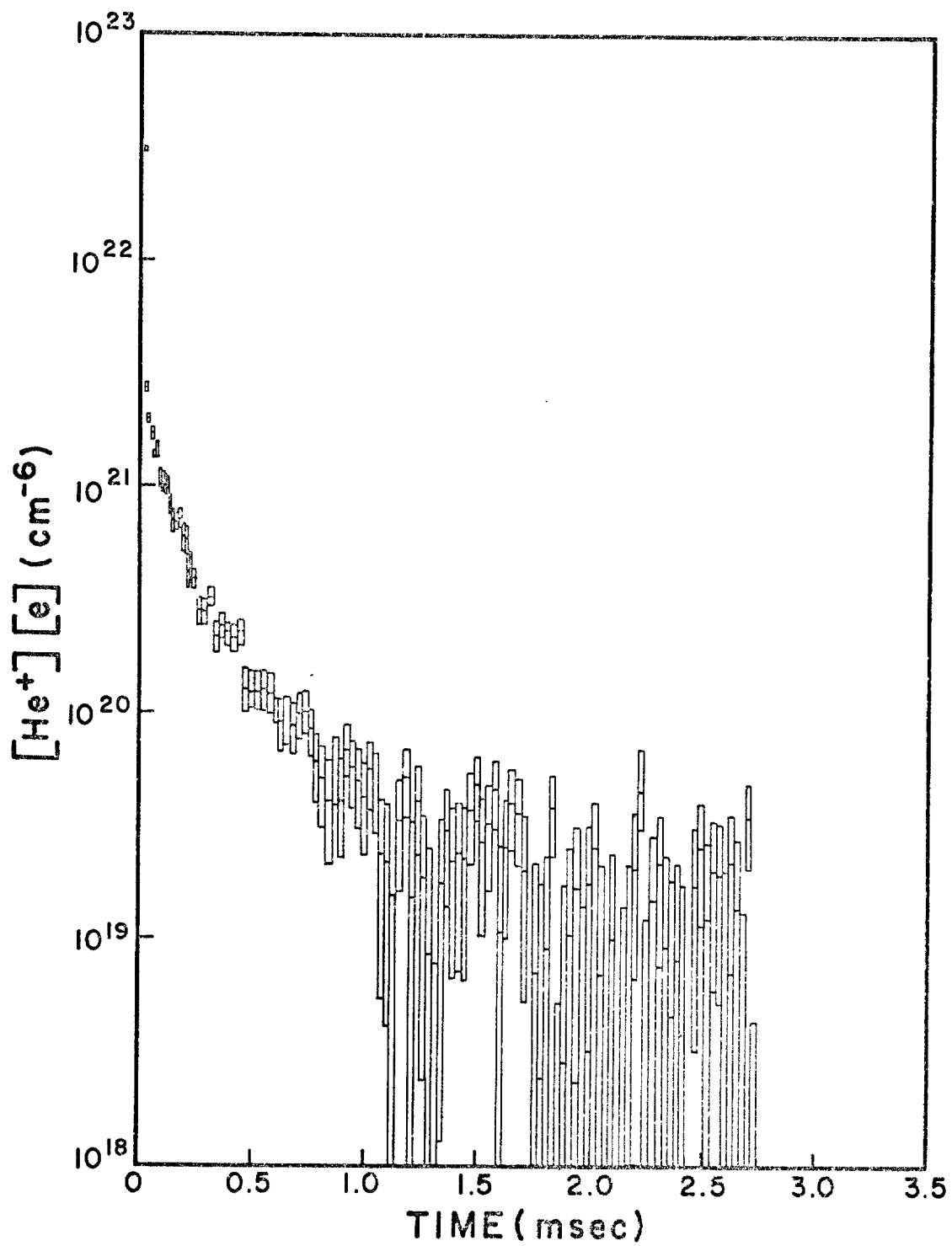


Figure 9

A graph of the recombination rate coefficient, α , in units of $\text{cm}^3\text{sec}^{-1}$, plotted as a function of time in msec.

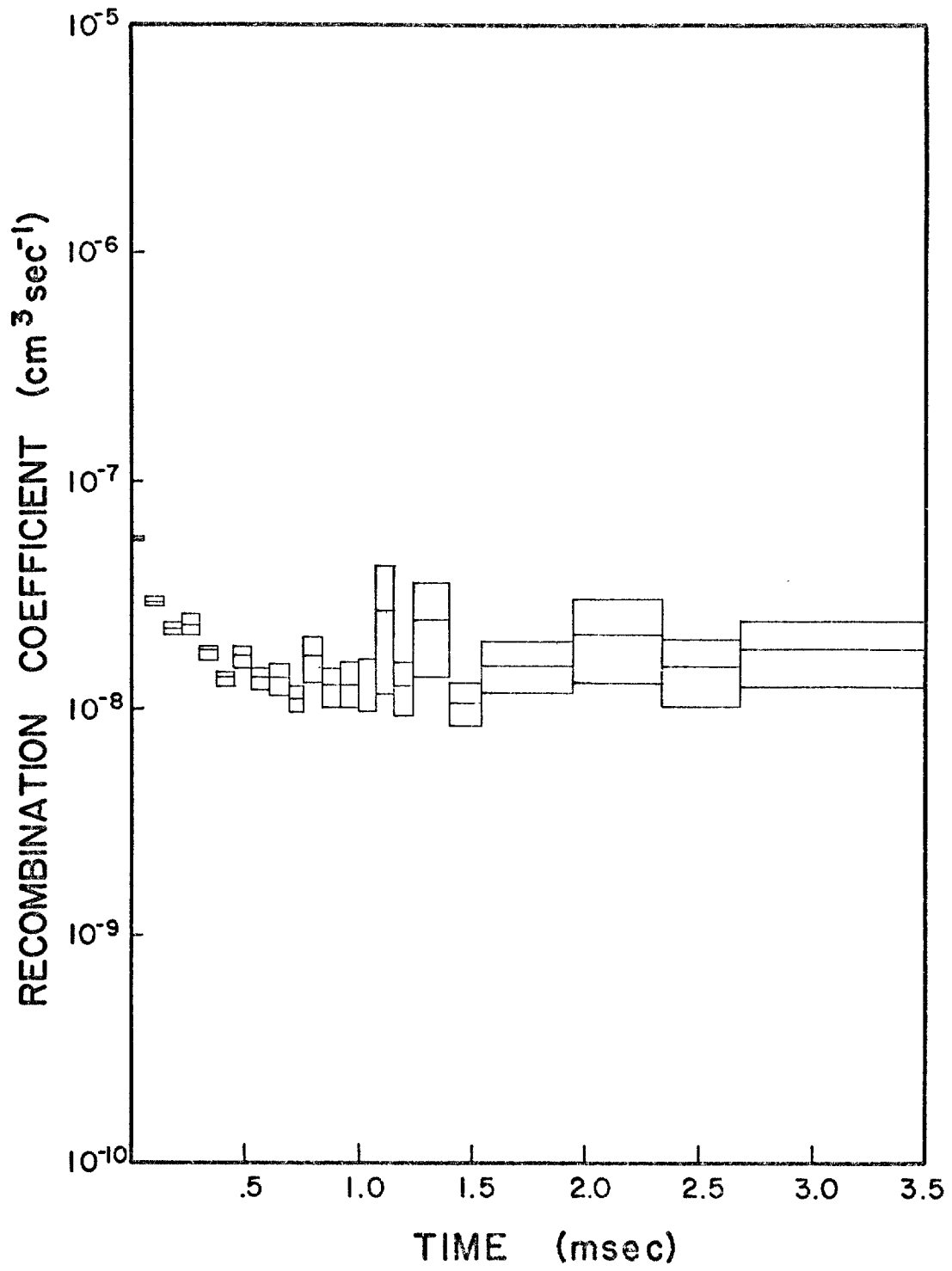


Figure 10

A graph of electron density in units of cm^{-3} versus time in msec, as determined by a 36GHz microwave interferometer.

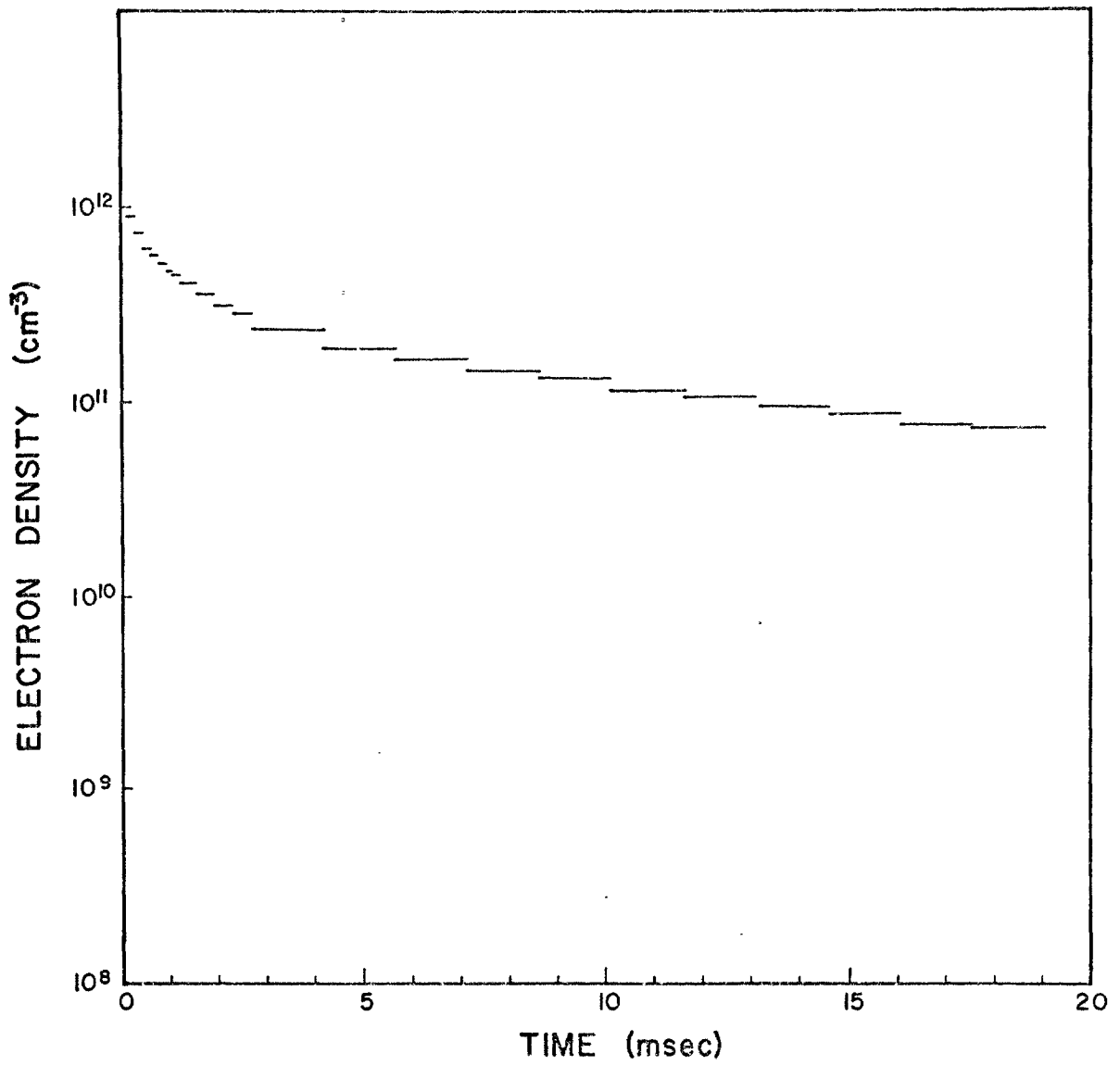
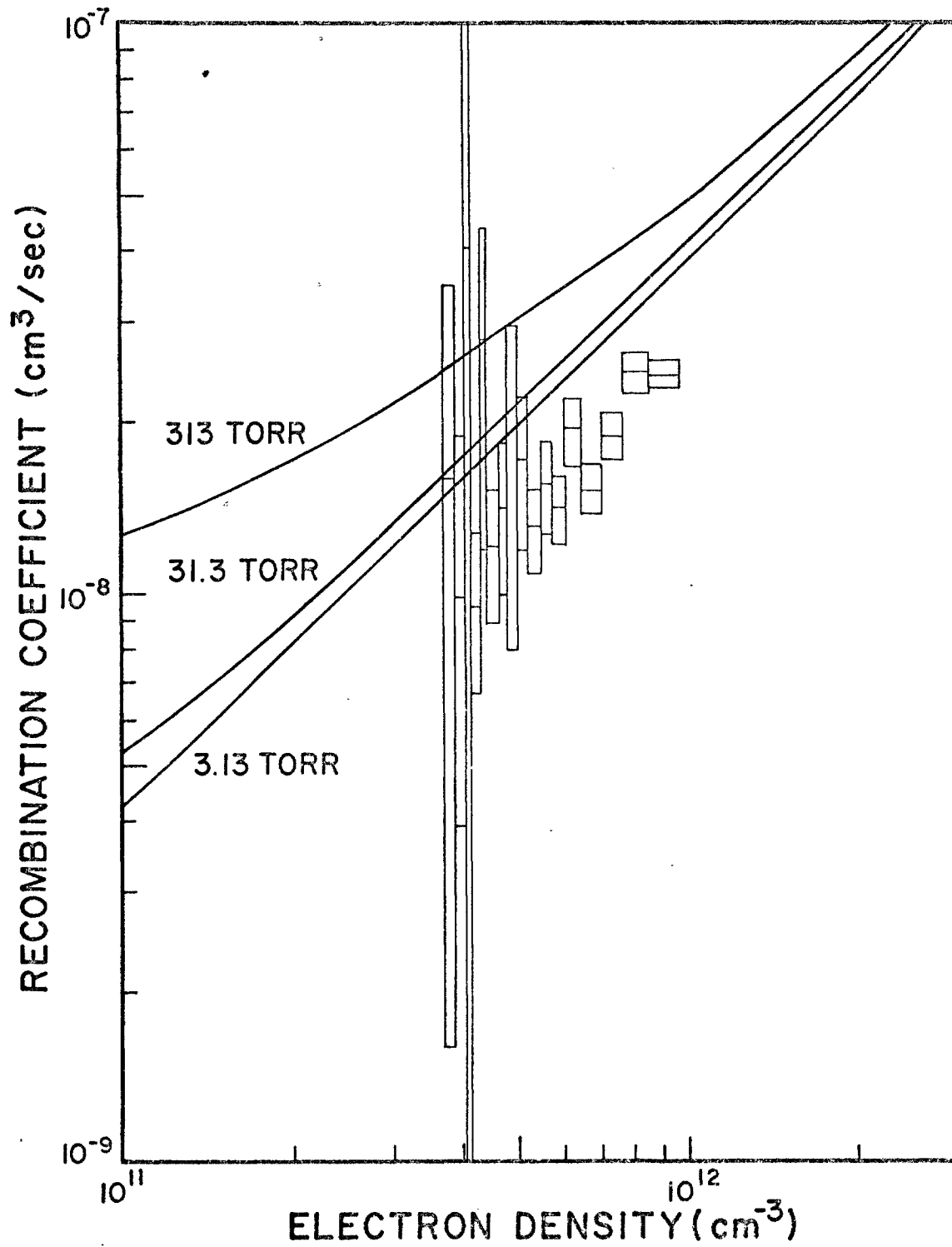


Figure 11

A graph of the recombination rate coefficient measured as a function of electron density, at a neutral gas pressure of 44.6 Torr. Shown for comparison are theoretical values, calculated as a function of electron density, for neutral gas pressures of 3.13, 31.3, and 313 Torr, reading from bottom to top, respectively.



CHAPTER VII

CONCLUSIONS

This work has presented an unambiguous measurement technique, which is nearly model-independent, for the determination of the recombination rate coefficient. Unlike the previous works of Born, and Deloche, Gonfalone and Cheret, no assumption as to the identity of the dominant ion present need be made, and all sources of internal ionization are contained in the determination of the recombination coefficient.

Data taken at a pressure of 44.6 Torr has been presented to demonstrate the feasibility of the measurement. At this pressure, radiation from the molecular helium recombination is much stronger than that from the atomic ion recombination. A severe demand is made on any measurement dependent on the weak radiation of the atomic ion recombination, by this high pressure characteristic. The success of the measurement at this pressure indicates the technique could be extended to even higher pressures.

The application of this method at other pressures should allow the accurate determination of the recombination coefficient over a range of electron densities, which, in turn, should indicate the relative importance of the

electron-induced and the neutrally induced recombinations discussed in Chapter II.

REFERENCES

1. E. W. McDaniel, Collision Phenomena in Ionized Gases, (Wiley & Sons, New York, 1964, p. 512).
2. D. R. Bates, A. E. Kingston and R. W. P. McWhirter, Proc. Roy. Soc. 267A, 297 (1962).
3. E. Hinnov and J. G. Hirschberg, Phys. Rev. 125, 795 (1962).
4. D. R. Bates, and S. P. Khare, Proc. Phys. Soc. (London) 85, 23] (1965).
5. C. B. Collins, Phys. Rev. 177, 254 (1969).
6. C. B. Collins and W. W. Robertson, J. Chem. Phys. 40, 2208 (1964).
7. C. B. Collins and W. B. Hurt, Phys. Rev. 177, 257 (1969).
8. C. B. Collins and W. B. Hurt, Phy. Rev. 179, 203 (1969).
9. J. A. Hornbeck and J. P. Molnar, Phys. Rev. 84, 621, (1951).
10. Reference 1, p. 392.
11. H. R. Griem, Plasma Spectroscopy, (McGraw-Hill, New York, 1964, p. 137).
12. G. K. Born, Phys. Rev. 169, 155 (1968).
13. R. Deloche, A. Gonfalone, and M. Cheret, C. R. Acad. Sci. Paris, 267, 934 (1968).

14. C. B. Collins and W. B. Hurt, Phys. Rev. 167, 166 (1968).
15. G. K. Born and R. G. Buser, Phys. Rev. 181, 423 (1969).
16. T. Holstein, Phys. Rev. 72, 1212 (1947).
17. L. S. Frost and A. V. Phelps, Excitation Functions and Rates for the Principal Levels in Helium, Westinghouse Research Report 6-94439-6-R3, May 24, 1957.
18. M. Gryzinski, Phys. Rev. 115, 374 (1949).
19. F. E. Niles, Compilation of Helium Transition Probabilities, Ballistic Research Laboratories, report 1354, February 1967.
20. A. L. Schmeltekopf, Cataphoresis in Helium-Neon Mixtures, (No. 63-1684, University of Texas, 1962).
21. M. A. Heald and C. B. Wharton, Plasma Diagnostics with Microwaves (Wiley & Sons, New York, 1965).

APPENDIX A

ABSOLUTE INTENSITY CALIBRATIONS

All spectroscopic measurements were calibrated by comparison to a standard source, traceable to the Bureau of Standards. This appendix describes this method of calibration.

The standard source intensity was represented by

$$N(\lambda) = (3.842 \times 10^{-16} / \lambda^5) \exp(-5.932 \times 10^4 / \lambda), \quad (29)$$

where $N(\lambda)$ is in units of $\mu\text{watts}/\text{nm}/\text{mm}^2/\text{ster}$ and λ is in units of cm.

This source was placed a length d in front of the spectrometer. Under these conditions, the energy, in watts, at the spectrometer is

$$E_r(\lambda) = 35.55 N_\lambda \Delta\lambda (W_i W_e) / 10d^2, \quad (30)$$

where $\Delta\lambda$ is the dispersion of the spectrometer, and W_i and W_e are entrance and exit slit widths, respectively. This can be represented as a photon flux, by


$$N_r(\lambda_o) = \frac{1.10}{\lambda_o^4 d^2} \times 10^2 W_i W_e \exp(-5.932 \times 10^4 / \lambda_o). \quad (31)$$

As shown in Figure 12, the standard source was observed in two positions, the reference position, and the calibration position, behind the cell. To observe the source in the reference position, the plane mirror was rotated, as

Figure 12

Diagram of calibration setup used to determine absolute intensity.

focusing
mirror



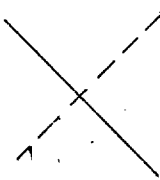
helium
cell

source

calibration
position

spectrometer

plane
mirror



source

reference
position

indicated by the dashed line position.

By observing the count rates, $C(\lambda_0)$, for the two positions, the photon flux from the calibration position, in terms of the photon flux from the reference position, is

$$N_c(\lambda_0) = [C(\lambda_0)/C(\lambda_0)]N_r(\lambda_0), \quad (32)$$

where the subscripts c and r refer to the calibration and reference positions respectively, and $N_r(\lambda_0)$ can be determined from equation (31).

For any wavelength λ , the photon flux from the calibration position, to the spectrometer, is

$$N_c(\lambda) = [N(\lambda)/N(\lambda_0)]N_c(\lambda_0), \quad (33)$$

or

$$N_c(\lambda) = [N(\lambda)/N(\lambda_0)][C_c(\lambda_0)/C_r(\lambda_0)]N_r(\lambda_0), \quad (34)$$

where $N(\lambda)$ and $N(\lambda_0)$ are determined by equation (29).

By observing the count rate, $C_p(\lambda)$, from the plasma, the photon flux arriving at the spectrometer can be represented by

$$N_p(\lambda) = [C_p(\lambda)/C_c(\lambda)]N_c(\lambda). \quad (35)$$

With this procedure, the cell radiation to the spectrometer was calibrated for all wavelengths measured.

By knowing the intensity of the radiation at the spectrometer, the total emission from the cell, per unit volume, was calculated by

$$I_p(\lambda) = [4\pi/\omega A]N_p(\lambda), \quad (36)$$

where ω is the solid angle of the focusing mirror, when subtended by the plasma, A is the cross-sectional area of the

plasma under observation, l is the length of the plasma, and equation (35) defines $N_p(\lambda)$.

When the relationship for lenses,

$$\omega_p A_p = \omega_s A_s, \quad (37)$$

where A_p is the area of the object and ω_p is the solid angle of the lens subtended at A_p and A_s is the area of the image, and ω_s is solid angle subtended at A_s , is applied to equation (36), then

$$I_p(\lambda) = [4\pi/\omega_s A_s l] N_p(\lambda), \quad (38)$$

where ω_s is the solid angle of the mirror subtended by the spectrometer, and A_s is the area of the slit.